POLYMER NANOENCAPSULATED SURFACTANT TEMPLATED AEROGEL CORE COMPOSITES FOR MULTIFUNCTIONAL APPLICATION

By

KAHKIT CHAN

Bachelor of Science in

Mechanical Engineering

Oklahoma State University

Stillwater, Oklahoma

2006

Submitted to the Faculty of the
Graduate College of the
Oklahoma State University
in partial fulfillment of
the requirements for
the Degree of
MASTER OF SCIENCE
JULY, 2009

POLYMER NANOENCAPSULATED

SURFACTANT TEMPLATED AEROGEL

CORE COMPOSITES FOR

MULTIFUNCTIONAL

APPLICATION

Thesis Approved:

Dr. Hongbing Lu

Thesis Adviser

Dr. Raman P. Singh

Dr. J. Keith Good

Dr. A. Gordon Emslie

Dean of the Graduate College

ACKNOWLEDGMENTS

I would like to thank a number of people who played a key role in this project:

Dr. Hongbing Lu served as my advisor in this project. He also supported me financially throughout this project and also during my graduate studies at Oklahoma State University. Besides, the generosity and appreciated guidance he has contributed to this project are wordless.

Oklahoma Center for the Advancement of Science & Technology for sponsoring the project.

Dr. Raman P. Singh served as my thesis committee member and has given me a lot of knowledge on composite from the Advanced Composite course.

Dr. J. Keith Good served as my thesis committee member and has given me the knowledge on finite element analysis.

All of my colleagues shared the most important thoughts and ideas during the group meeting. Special thanks go to Boshen Fu on finite element analysis and Kaylan Vengala on acoustic test.

I would like to thank all of my family members for their support and encouragement, especially my parents. Last but not least, I would also like to thank my wife and a year old son for their priceless support and I also need to apologize for not having enough time at home or just staying in front of a computer typing all the time.

TABLE OF CONTENTS

Chapter Page

LIST OF TABLES

Table Page

LIST OF FIGURES

Figure Page

Figure Page

CHAPTER I

INTRODUCTION

1.1 Background

Aerogels are low-density, highly porous, nanostructured materials (Pierre and Pajonk, 2002). There are primarily three types of aerogels: inorganic, organic and carbon aerogels. Inorganic aerogels are formed by supercritical fluid (SCF) drying of wet gels (i.e., solvent-filled gels) synthesized through a sol-gel process by hydrolysis and polycondensation of metal and semimetal alkoxides. During SCF drying, gelation solvents are first replaced by liquid CO2 that is taken supercritical (i.e. above the critical point of CO2) and is vented off. Among inorganic aerogels, silica aerogels are the most well-known. However, their engineering application is very limited due to extreme brittleness and hydrophilicity (Fricke, 1988; Woignier and Reynes, 1998; Pierre and Pajonk, 2002; Miner and Hosticka, 2004). The aerogel fragility is traced to the weak links in the aerogel skeletal framework, which are the inter-nanoparticle necks in the 'pearl-necklace' network structure. Based on the premise that polymer-nanoparticle composites show properties above and beyond those of the individual components (Thayer and Houston, 2003), recently a new kind of strong lightweight aerogel was developed by encapsulating the skeletal aerogel nanoparticles under a thin (~2 nm thick) layer of

polymer (Leventis et al., 2002, 2005; Zhang et al., 2004; Bertino et al., 2004; Meador et al., 2005; Katti et al., 2006). Polymers such as polyurethanes, polyureas, epoxies and polystyrene, coat conformally the surface of the aerogel skeleton, thus retaining the mesoporous structure while the interparticle necks get wider. The process that furnishes the new material is referred to as crosslinking and the new material is referred to as crosslinked silica aerogel (CSA). The polymer crosslinked aerogel (X-Aerogels) can be up to three times more dense, but more than 300 times stronger, and less than one tenth as hydrophilic as native aerogels. With low thermal conductivity, high acoustic damping, ease in fabrication, X-Aerogels has potential in engineering applications as lightweight structural materials. Thus, the characteristic of aerogels as core material in sandwich structures were investigated in this paper.

Sandwich constructions have been widely used in different applications in many areas. These high strength-weight ratio structures have been slowly replacing monolithic materials in many engineering applications. It goes even further as certain mechanical and bulk properties can be tailored to properties not yet available in a single material. Sandwich structures can be designed to have addressed the needs in many applications. The flexibility of designs can range from the number and orientation of plies in the face sheets, the thickness of the core in the sandwich structure and more importantly, the different core materials used.

In a sandwich construction, it consists of at least two plies of faces sheet, top and bottom face sheets sandwiching a core. The common face sheet materials in the structures

contain two or more distinct constituent materials or phases known as composite. The commonly used composite materials are plastics, woods and metals. As for the core material, metal in the form of foam or honeycomb, and Nomex paper in the form of honeycomb are the most widely used in the primary structural application.

The sandwich constructions involved combination of different materials and each material will give advantage and disadvantage to the mechanical properties. For example, some of the critical factors are the bonding strength between the face sheets and core, buckling of sandwich structure and composite, etc. Among all of these factors, failure modes are always reported in composite testing as failure loads are closely related to failure modes.

In this study, Nomex honeycomb and a highly porous low-density material known as corosslinked aerogels were used as the core material in a sandwich construction. The aerogel used in this work was polyurea crosslinked surfactant templated silica aerogel, designated as X-MP4-T045 with high compressive strength [2]. A study was conducted with using three different types of cores, which are Nomex honeycomb, crosslinked aerogel embedded in Nomex honeycomb, and crosslinked aerogel core. In this paper, as for convenience in writing, the Nomex honeycomb, crosslinked aerogel embedded in Nomex honeycomb and crossljnked aerogel are designated as honeycomb, H-X-MP4-T045 and X-MP4-T045 respectively.

1.2 Literature Review

Traditional silica aerogels were invented in the 1930's by Steven S. Kistler .He proved that a gel contained a continuous solid network with the same size and shape as the wet gel by replacing the liquid with air without damaging the solid components (Kistler 1998). Silica aerogels are known as the lightest solid on earth with a mass density of 1.0 mg/cm^3 [3]. However, silica aerogels are very brittle due to the weak links between neighboring secondary particle and could act as a strong desiccant due to its high porosity, high surface area and hygroscopic nature. There is a renewed interest in aerogels because of the demand in light weight and material with good thermal insulation material. In recent years, aerogels has been used as material to thermally insulate electronic box on board of Mars Rovers where temperature reached can be as low as -40°C [4]. Silica aerogels has also been used to collect space dust in NASA's Stardust Program.

Figure 1.1. Traditional Silica Aerogel, Stardust Program, JPL website.

Traditional aerogels are brittle, fragile and hygroscopic. To resolve these issues, Dr. Leventis modified silica aerogels by cross-linking with secondary particles [3]. His results showed that cross-linked silica aerogel may take more than 300× the force to break and the density is increased only by 3× [3]. Traditional silica aeroges are produced by replacing the liquid component of the gel to gas by supercritical drying which normally resulted in slight shrinkage. Through this process, the gel has greatly reduced its weight by having more than 99% of internal void space [3]. Also, aerogels are inherently fragile and environmental sensitive, crosslinking the mesoporus silica structure of an aerogel will enhance the property of aerogels and experiment has shown that the stress at failure was 120 times higher than traditional aerogels [2].

Schmidt and Schwertfeger investigated silica aerogel as thermal and acoustic insulation material [5]. The results showed that aerogel has outstanding performance and as the porosity of aerogel increases, the thermal insulation capability increases. The thermal properties of a composite can be influenced by adding aerogel and this effect can be used for the construction of insulation plates for combined thermal and footfall insulations [5]. This is due to the fact that aerogels of mesoporous reducing voiding convection, conduction and radiation. As for measure for the sound insulation performance, aerogels show high acoustic damping [3]. Aerogels were reported to have the ability to absorb 90% of the sound in the frequency range between 4-5 kHz [5]. Also, as the thickness of the aerogels increase, the value at the high frequency decreases but it moves toward to low frequencies with 60% sound absorption capability at frequency range between 650 Hz and 1 kHz. Traditional insulation materials show significant

decrease in sound insulation at lower frequency range [5]. In order to obtain better results in this area, many researchers have modified aerogels by varying the solvent with different volume concentration [2, 3]. In some applications, aerogels can be used directly but most of the times when the requirement of mechanical strength is high, aerogels are used with other materials with higher mechanical strength and toughness [5].

1.3 Scope of this work

In this work, processes are developed to prepare aerogel composite sandwich structure to provide multifunctionality. The aerogel sandwich structures will be characterized to determine their acoustic and mechanical properties. The sound absorption coefficient and sound transmission loss are measured by an impedance tube, with the use of two and four microphones set-up, an oscilloscope and a noise generator. The measurement of sound absorption coefficient follows the ASTM E-1050 standard and sound transmission loss in “Measurement of transmission loss of materials using a standing wave tube” by Oliviero Olivieri, J. Stuart Bolton and TaewookYoo [1] that is similar to ASTM E-1050.

For mechanical testing, flexural test was used to evaluate the strength and stiffness of aerogel composite structure in three point bending. The results are compared with conventional Nomex core composites. Experimental data are compared with analytical and numerical results.

CHAPTER II

FABRICATION

2.1 Polymer Crosslinked Aerogels

The pre-preg FSG 584 (unidirectional woven carbon fiber) embedded F155 resin were provided by Hexcel Composites (Bedford, TX 76022) and 3 lb density Nomex honeycombs were purchased from Applied Vehicle Technology (Indianapolis, IN 46218). Polypropylene molds were purchased from Melmatinc, model number (P-084). Acetone, acetonitrile, and alcohol were all purchased from Pharmaco Chemical Company (Brookfield, CT 06804), Nitric acid was purchased from Seastar Chemical Inc. (Pittsburgh, PA 15275), tetramethylorthosilicate (TMOS) and 1.3.5-trimethylbenzene (TMB) were purchased from Sigma-Aldrich (St. Louis, MO 63103), and Pluronic P123 (tri-block co-polymer: $PEO_{20}PPO_{70}PEO_{20}$) was supplied by Acros Organics (New Jersey). Research samples of Desmodur N3200, a hexamethylene diisocyanate oligomer, were provided by Bayer (Pittsburgh, PA 15205).

2.2 Preparation of Crosslinked Aerogels

The aerogels used in this study were synthesized using the same procedures as used by Leventis group. They are labeled following Leventis notation [3]. For example, for aerogel as X-MP4-T45, 'X' indicates crosslinked, 'P4' and T45 stand for 4 g of Pluronic P123 and 0.45g of TMB, respectively. In this procedure, 4.0 g of Pluronic P123 ($C_5H_{10}O_{2)}$ was dissolved in 12 g of 1.0 M aqueous solution of nitric acid (HNO_3) under magnetic stirring for 8 hours. Under vigorous stirring, 0.45 g of Tetramethylbenzidine known as TMB ($C_{16}H_{26}Cl_2N_2O_2$) was added to the solution for 30 min. The solution was cooled to 0°C and 5.15 g of Tetramethoxyl silane known as TMOS $Si(CH_3)_4$ was added to the solution after another 30 min.

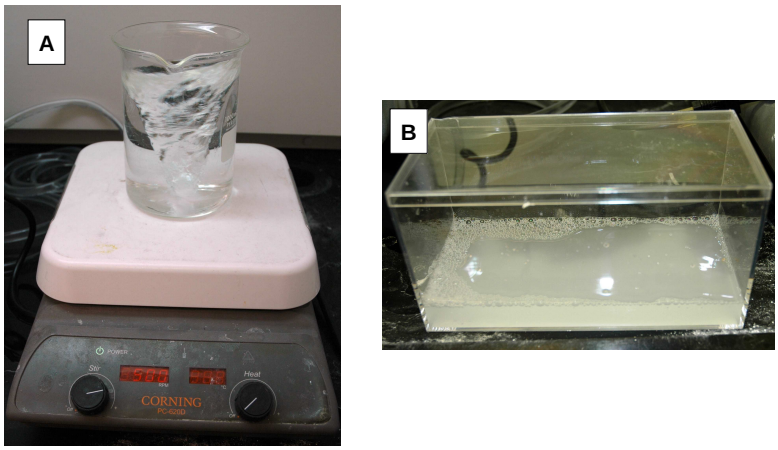

Figure 2.1. (A) Sol solution under vigorous stirring before pouring to the (B) polypropylene mold.

The pre-cooling was to avoid crosslinker TMOS to react quickly with other agents and this is due to the boiling point of TMOS which is 26.6C. Mixing the two agents at

room temperature would lead to an increase in temperature which will result in gelation being immediately taken place before the solution was thoroughly mixed. After stirring for 10 min, the solutions were poured into a polypropylene mold. The mold was then closed with the lid, sealed with PTFE tape to avoid evaporation of the liquid and kept inside the oven at 60 °C for gelation. The sample was monitored every 10 to 15 min until gelation was complete and the sample was then aged at 60°C for 5× the gelation time which was about 12 h. The wet gel was removed from the mold and placed into ethanol with the amount of 4× the volume of the gels to remove residual water. At this stage, the wet gel is extremely fragile. Ethanol was changed 2× at 8 h intervals. The sample went through Soxhlet extraction which is similar to distillation process by using CH_3CN as solvent for 2 days to remove P123. Recent results from Dr Letentis group show that the pre-crosslinking washes may be eliminated but to get the sample which is identical to the previous work, the wet gel was washed. Acetone was used to wash the sample 4× with 8 h intervals. After washing with acetone, the sample was crosslinked with acetone solutions of the diisocyanate (Desmodur N3200).

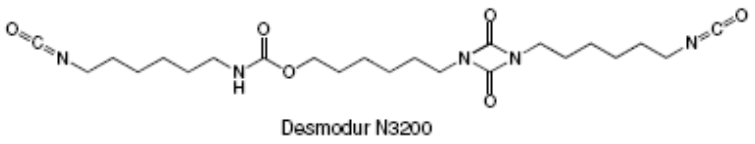

Figure 2.2. Chemical compound of crosslinker Desmodur N3200.

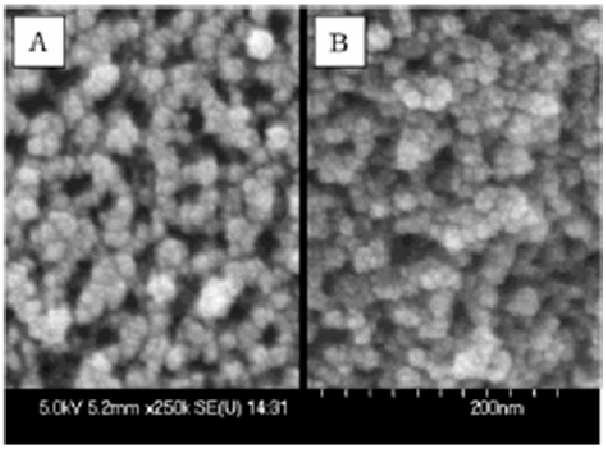

Figure 2.3. SEM micrographs for native silica (left) and crosslinked aerogel (right).

The volume of the solution was 4× greater than volume of the sample with the ratio between acetone and N3200 of 12 g to 88 ml. After the Desmodur N3200 solution had reached the equilibration time (1 day) at room temperature, the sample, together with the Desmodur N3200 solution, was heated at 55°C for 3 days. Acetone was used again to wash the sample 4× with 8 h intervals to remove the unreacted diisocyanate. Finally, the sample was dried with Penthane to get X-linked monolith.

The dark areas represent mesoporosity. Native silica aerogel consists of 95% of void space and after crosslinking process, the void space reduces to 70%.

Figure 2.4. Crosslinked silica aerogel.

2.3 Aerogel Embedded in Nomex Honeycomb

In order to increase the performance in mechanical strength and acoustic insulation, aerogels embedded into honeycomb was used as a core material. There are two ways to embed crosslinked aerogels into the Nomex Honeycomb. In the first approach was placed a piece of honeycomb in the polypropylene mold before the solution was poured into the mold. The solution would fill the cavities of the honeycomb, and the gelation will occur inside each cells of the honeycomb.

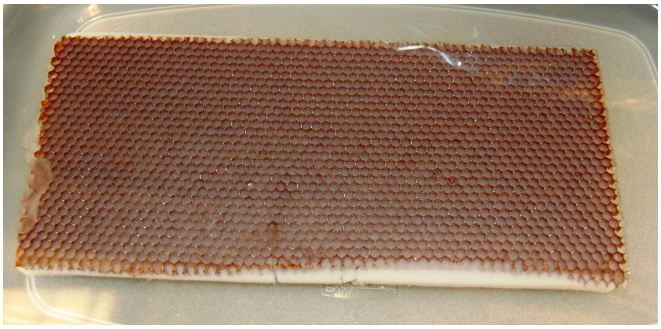

Figure 2.5. Gelation of aerogel inside the Nomex Honeycomb.

In the second approach a piece of wet gel was pressed into the honeycomb cells. This requires the piece of crosslinked aerogel to have the same thickness as the honeycomb to prevent damage to the aerogel inside the cell. After washing and curing the wet gel with all the chemicals, crosslinked aerogels were formed inside each cell of the honeycomb. The tiny hexagonal crosslinked aerogels were then transferred into a new honeycomb to avoid any potential structural damage to the honeycomb during the washing process.

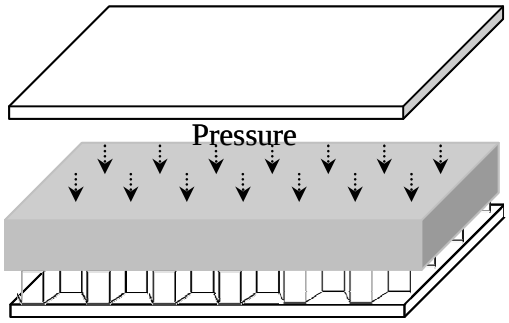

Figure 2.6. Soft gel being pressed into the Nomex Honeycomb.

The hexagonal crosslinked aerogel which were formed inside the honeycomb mold were removed and placed into a larger piece of Nomex Honeycomb for easiness of composite layup. Figure 2.7 shows a Nomex honeycomb with hexagonal cavities filled with crosslinked aerogels.

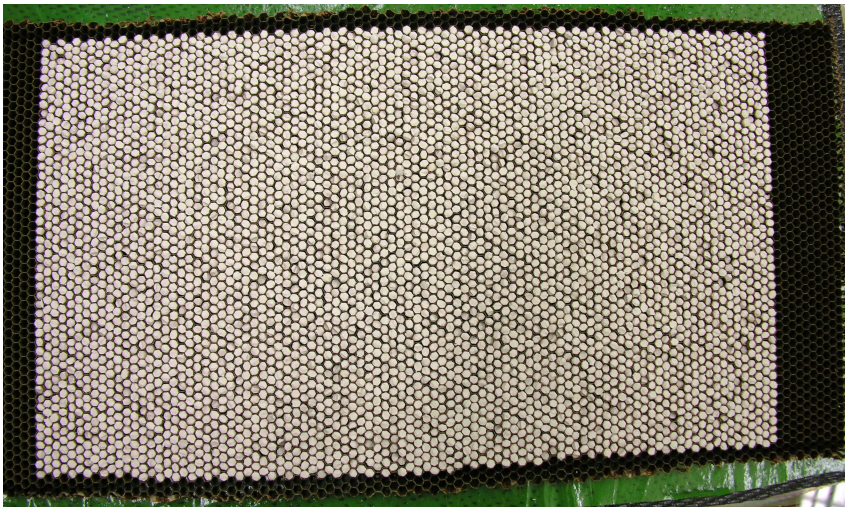

Figure 2.7. Honeycomb embedded X-MP4-T45.

2.4 Composite Lay-up

FSG 584 unidirectional carbon fiber reinforced F155 resin matrix is a low to medium viscosity prepregs formulated to oven cure at low temperature for 12 hours which specifically chosen to match the allowable temperatures without changing the properties of the X-MP4-T45. The glass transition temperature of X-MP4-T045 is about 120 °C. Honeycomb, H-X-MP4-T045 and X-MP4-T45 were the core materials for evaluation of the acoustic and mechanical properties in this study. The composition for the fiber and reinforcement by weight provided in the product data sheet by (Hexcel Composites) are 56.62% (fiber) and 43.38% resin, respectively. A thin layer of LTA26EL adhesive was applied to both sides of the core to allow the face sheets (pre-pregs) to bond to the core. The sandwich structure were placed in between two glass plates covered with vacuum bagging film and breather while applying 26 inHg vacuum pressure at room temperature within the bag. The sandwich and glass assembling was then heated to 80 °C

at temperature rate 1°C/m and maintained at 80 °C for 12 h. The temperature was then slowly lowered to room temperature while maintaining the 26 inHg vacuum pressure. At room temperature, the vacuum is removed and the sandwich was complete.

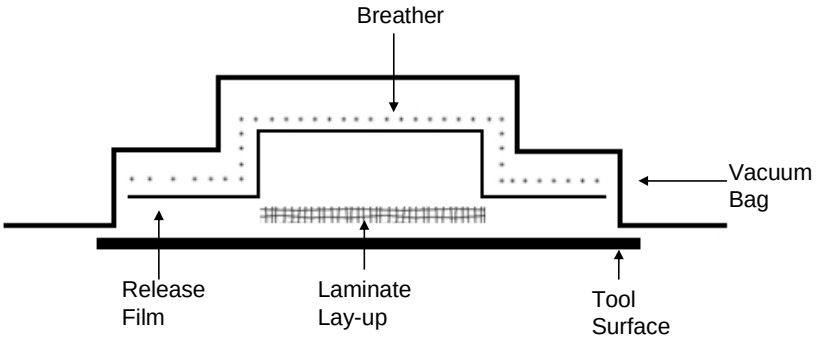

Figure 2.8. Bagging arrangement for composite lay-up.

2.5 Testing Specimen Preparation

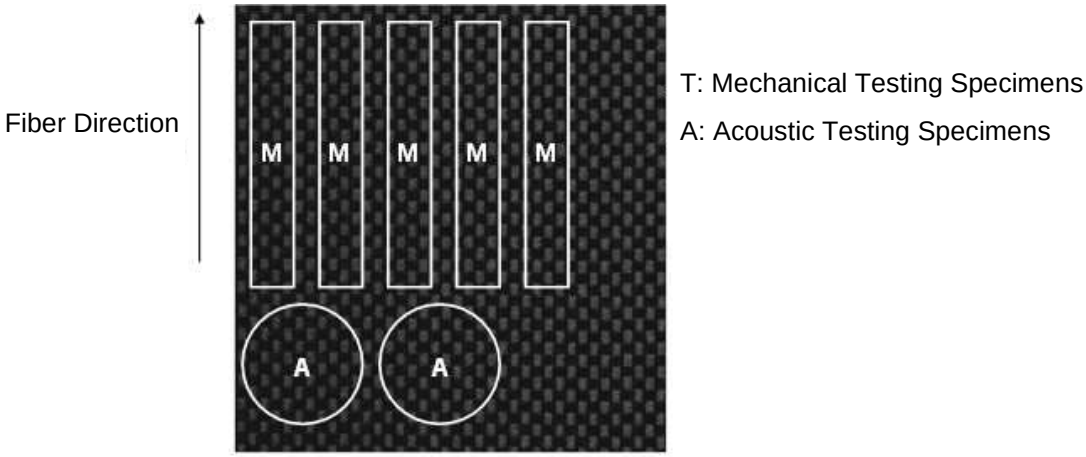

Figure 2.9. Test specimens cut from laminate.

All the specimens for mechanical testing were cut along the fiber direction which is known as the longitudinal direction for all the flexural test specimens. For each types of core composites, five specimens for flexural tests and two specimens for acoustic tests were prepared. A saw and a milling machine using diamond grid hole saw were used to cut the specimens for flexural and acoustic tests, respectively. The diamond grid hole saw was manufactured by McMaster-Carr with model number (6930A48), it is appropriate to cut composite such as Kevlar and carbon fiber. The sides of the specimens were polished with sand paper to reach a smooth surface.

Table 2.1. Specimen dimensions for flexural and acoustic tests; number in parentheses indicates standard deviation.

Flexural Test				
Core	**L (mm)**	**b (mm)**	**t (mm)**	**ρ (g/cm^3)**
Honeycomb	165.89 (3.02)	33.64 (0.55)	8.63 (0.144)	0.53 (0.01)
H-X-MP4-T045	154.17 (1.66)	34.41 (1.08)	9.07 (0.15)	0.83 (0.01)
X-MP4-T045	151.95 (0.59)	34.36 (0.47)	8.93 (0.02)	0.95 (0.03)
Acoustic Test				
Core	**d (mm)**	**t (mm)**	**ρ (g/cm^3)**	
Honeycomb	53.82 (0.12)	8.45 (0.13)	0.55 (0.01)	
H-X-MP4-T045	53.90 (0.05)	9.57 (0.15)	0.77 (0.01)	
X-MP4-T045	54.00 (0.01)	8.636 (0.11)	0.99 (0.01)	

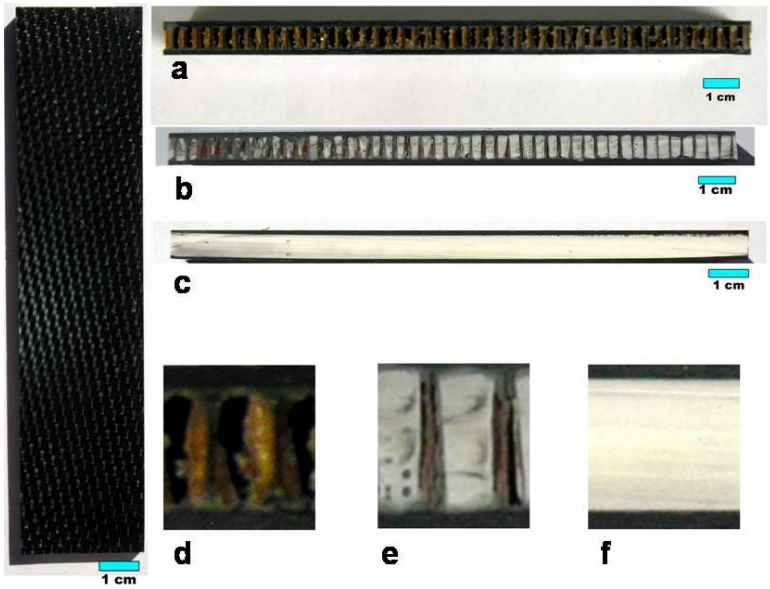

Figure 2.10. Flexural test specimens with different cores material (a) honeycomb, (b) H-X-MP4-T45 and (c) X-MP4-T45 and (d), (e) and (f) are the zoom in view for (a), (b) and (c) respectively.

Figure 2.11. Acoustic test specimens

The dimensions for the flexural specimens followed the ASTM D790 standards. The specimen's length for mechanical testing is about 16 times of the thickness. Some specimens were slightly shorter due to the limitation of the polypropylene mold used to fabricate X-MP4-T045, but the error difference from the standard length/thickness ratio is within 5%. The width of the specimen is below four times of the thickness of the

specimen. The diameter of the acoustic testing was slightly smaller than diameter of the impedance tube to ensure a good seal. Table 2.1 shows the dimensions of all the specimens for mechanical and accosting testing. L, b, t and ρ indicate the length, width, thickness and density of the specimens respectively.

CHAPTER III

MECHANICAL CHARACTERIZATION

3.1 Three-point Bending Experiment

An MTS 810 materials testing system retrofitted with an Instron digital controller and data acquisition system was used for the flexural test. The load and displacement data were recorded simultaneously as a function of time. A 5 kN load cell was used for the entire testing. The testing span length, L, as well as the length/thickness ratio follows the ASTM D790. The span length, L= 133.35 mm was chosen for all flexural specimens.

Flexural properties of sandwich construction were calculated using elementary beam theory. The flexural strain was calculated with respect to the deflection of the outer surface of the test specimen at midspan using

$$\varepsilon_f = 6Dd / L^2 \tag{3.1}$$

where ε_f is the strain, on the top face sheet, D is the maximum deflection at the center of the beam, L is the support span length, and d is the thickness of the specimen.

For flexural test, the maximum stress occurs at the midpoint of the specimen. The stress was calculated from the load at the midspan of the outer surface of the test specimen using

$$\sigma_f = 3PL / 2bd^2 \quad (3.2)$$

where σ_f is the stress on the outer fibers at midpoint, P is the load at the midpoint, and L is the support span length, d is the thickness of the specimen and b is the width of the specimen.

The modulus of elasticity was determined using the initial straight line slope of the load-deflection curve using

$$E_f = L^3 m / 4bd^3 \quad (3.3)$$

where E_f is the modulus of elasticity, m is the slope of the load-displacement cure, L is the support span length, d is the thickness of the specimen, and b is width of the specimen.

3.2 Results and Discussions

The flexural properties and load-displacement curves for honeycomb, H-X-MP4-T045 and X-MP4-T45 cores are shown in Table 3.1 and Figure 3.1, respectively. Five specimens were tested for each type of core material and the average value was obtained with standard deviation reported in the parentheses. Observation of the testing showed

that the failure occurred on the outer surface of the specimen after the honeycomb core failed.

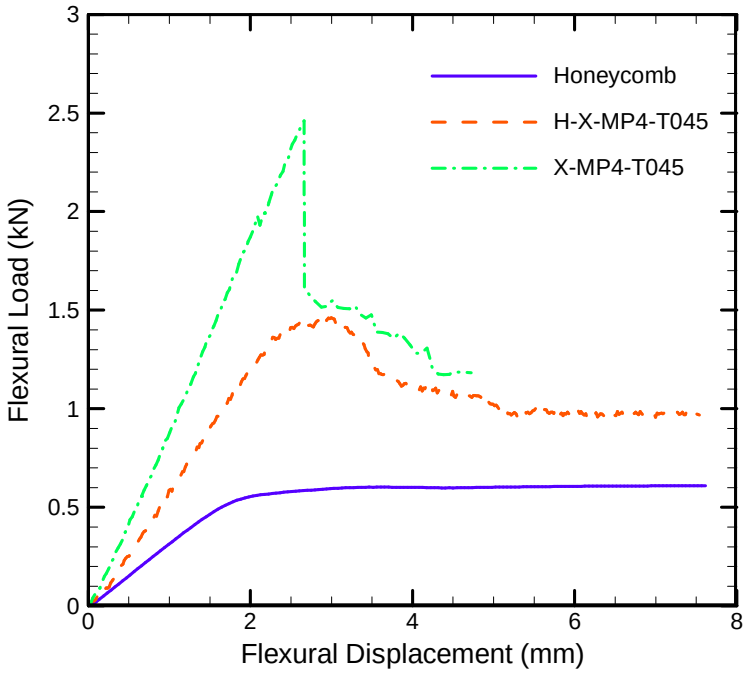

Figure 3.1. Flexural load-displacement curve.

In testing the H-X-MP4-T45 core, the breaking sound of hexagonal crosslinked aerogels inside cells of the honeycomb was observed during the experiment after the load had reached around 500 N. The peak was corresponded to the failure of the crosslinked aerogels. It is reasoned that initially the load was applied on the entire structure and when the deflection had reached a certain load, tension and compression within the structure as well as wrinkling in the honeycomb (Choon Chiang Foo, Gin Boay Chai, Leong Keeh Seah) occurred which resulted in fracture of the crosslinked aerogels within hexagonal cells of the honeycomb core. When the load reached 1500 N, it yielded about 6 mm

deflection before failure. Failure occurred for the H-X-MP4-T045 core with failure mode similar to that of honeycomb comb. Fracture of the sandwich occurred at a mid-span deflection of about 9 mm on the face sheet for honeycomb and X-MP4-T045 cores.

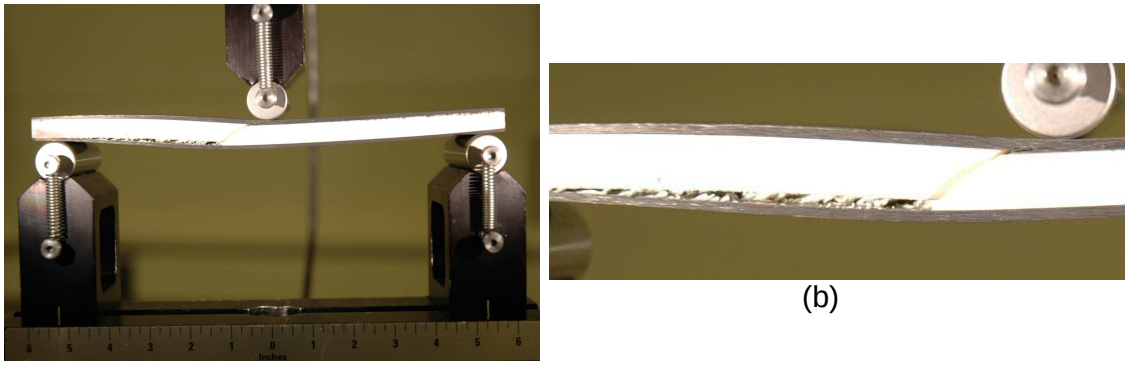

(a) (b)

Figure 3.2. (a) Flexural test on MP4-T45 core and (b) failure and debonding between the core and the face sheet.

However, failure first occurred in the plain crosslinked aerogel core, X-MP4-T45 at 2 mm mid-span displacement with 2500 N ultimate load. It appeared that crosslinked aerogels failed in brittle mode due to its low flexibility because of the mesoporosity. Figure 3.2(b) shows the delamination and debonding were immediately occurred after the X-MP4-T045 core failed near the mid-span.

Table 3.1. Flexural properties data.

Cores	Density (g/cm^3)	Specific Flexural Strength (MPacm3g-1)	Flexural Modulus (GPa)
Honeycomb	0.53 (0.01)	89.11 (1.46)	8.11 (0.35)
H-X- MP4-T45	0.83 (0.01)	107.04 (14.27)	14.43 (1.03)
X-MP4-T45	0.95 (0.02)	168.95 (24.74)	23.12 (0.60)

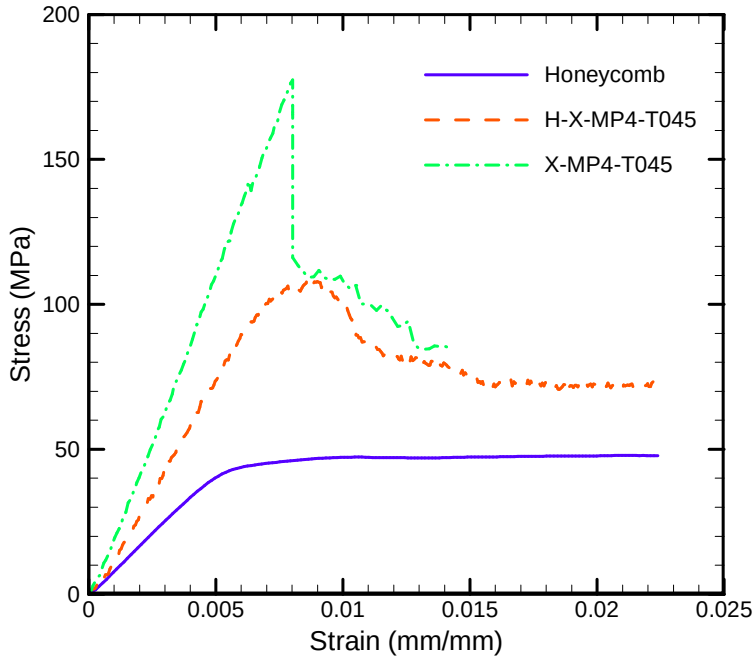

Figure 3.3. Flexural stress-strain curve.

X-MP4-T045 has the highest flexural modulus and ultimate flexural strength. However, the X-MP4-T045 failed at 0.08% of strain before yielding. For H-X-MP4-T045, the bulk density of the sandwich structure increased by 35% and the flexural modulus and the ultimate flexural strength increased by 40% and 46.84%, respectively when compared

to the honeycomb core composite. Also, the flexural modulus and flexural ultimate strength were decreased by 37.5% and 44.6% when compared to the X-MP4-T045 but it resisted more flexural strain before failure.

3.3 Analysis

In this section, elementary beam analysis is used to evaluate the modulus of the composite. The elementary beam theory, as adapted to sandwich beams was used. In elementary beam theory, flexural rigidity is the product of the Young's modulus, E, and the beam's moment of inertia about the neutral axis. In this case, the flexural rigidity is the summation of the values of different layers, measured from the neutral axis.

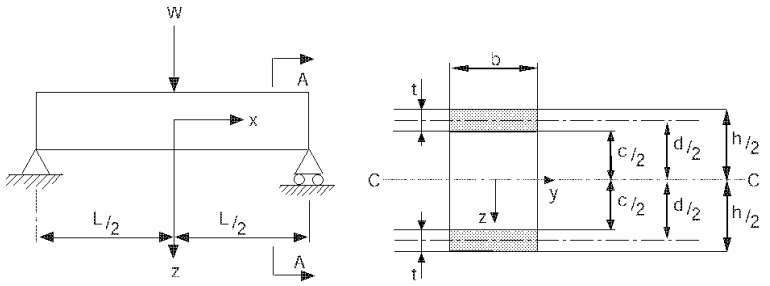

Figure 3.4. Description of a laminate geometry [6].

E_f and E_c denote the elastic modulus values of the face sheet, and the core, respectively; b and t are the width and thickness of the face sheet, respectively; c and d are the thickness of the core and measurement of the centroid axis between the top and bottom face sheets, respectively. The flexural rigidity is defined as

$$D = E_f \frac{bt^3}{6} + E_f \frac{btd^2}{2} + E_c \frac{bc^3}{12} \tag{3.4}$$

where

D= flexural rigidity, Nmm^4

t= thicnkness of the face sheet, mm

b = width of the sandwich beam, mm

d = length of centroid axis between top and bottom face sheet, mm

E_f = elastic modulus of the face sheet, MPa

E_c = elastic modulus of the core material, MPa

In order to simplify the equation, the first and third term of the flexural rigidity can be ignored if the following is satisfied.

$$\frac{d}{t} > 5.77 \tag{3.5}$$

The first term is involved of the thickness of the face sheet. If the face sheet is thin when compared to the sandwich structure, the first term can be canceled and the equation can be reduced to

$$D = E_f \frac{btd^2}{2} + E_c \frac{bc^3}{12} \tag{3.6}$$

$$\frac{E_f}{E_c} \cdot \frac{td^2}{c^3} > 16.7 \tag{3.7}$$

The third term can be ignored if the equation satisfied the condition in Eq. (3.7), the flexural rigidity of the sandwich structures is reduced to

$$D = E_f \frac{btd^2}{2} \tag{3.8}$$

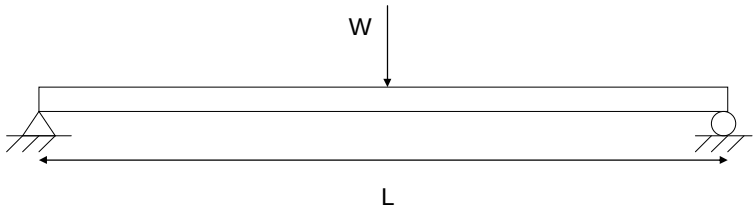

Figure 3.5. A simply supported three-point ending with a concentration load applied at the center.

All of the three cores material used in this study satisfied Eq. 3.5 and Eq. 3.7. Thus, the flexural rigidity was reduced to Eq. 3.8. After simplifying the equations for the beam and sandwich beam (Eq. 3.3 - Eq. 3.8), the flexural modulus of the sandwich beam is defined as

$$E = \frac{6L^2 d^2 t_f E_f G_c}{t_c^3 (G_c L^2 + 6E_f t_f d)} \tag{3.9}$$

where

E = flexural modulus, MPa

L = span length of the sandwich beam, mm

b = width of the sandwich beam, mm

d = length of centroid axis between top and bottom face sheet, mm

t_c = thickness of the sandwich beam, mm

t_f = thickness of face sheet, mm

E_f = elastic modulus of the face sheet, MPa

E_c = elastic modulus of the core material, MPa

G_c = shear modulus of the core material, MPa

The shear modulus of the H-X-MP4-T045 follows the equation to calculate the shear modulus of composite material. However, this equation is limited to two material constituents in the composite. The equation is defined as

$$G = \frac{G_A G_H}{G_H V_A + G_A V_H} \tag{3.10}$$

$$v = v_H + v_A \tag{3.11}$$

$$V_H = \frac{v_H}{v} \qquad V_A = \frac{v_A}{v} \tag{3.12}$$

where

G = shear modulus of the core, MPa

G_H = shear modulus of Nomex honeycomb, MPa

G_A = shear modulus of aerogel, MPa

V_H = volume fractions of honeycomb, ratio

V_A = volume fraction of aerogel, ratio

v = total volume of the core, mm^3

v_H = volume of honeycomb, mm^3

v_A = volume of aerogel, mm^3

The shear modulus for X-MP4-T045 followed generalized Hooke's law as shown in Eq. (3.13). The shear modulus for Nomex honeycomb is a combination of Gibson and Ashly [7] and generalized Hooke's law and is defined as

$$G_c = \frac{E_A}{2(1+\upsilon)} \tag{3.13}$$

$$E_H = \frac{\frac{E_S(1+\sin\theta)}{\cos^3\theta}\left(\frac{t}{l}\right)^3}{2(1+\upsilon)} \tag{3.14}$$

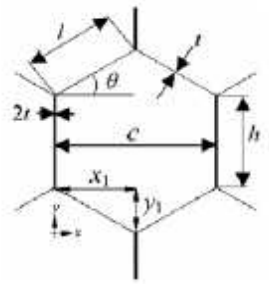

Figure 3.6. Geometrical parameter of a unit honeycomb.

where

G = shear modulus of the core material, MPa

Ec = flexural modulus of X-MP4-T045, MPa

ν = poisson's ratio

E_H = flexural modulus of honeycomb, MPa

Es = global elastic modulus of honeycomb, MPa

t = wall thickness of honeycomb, mm

l = side length of honeycomb, mm

Table 3.2. Flexural modulus (GPa) of the theoretical result on modulus for honeycomb, H-X-MP4-T045 and X-MP4-T045 cores.

	Honeycomb	**H-X-MP4-T045**	**X-MP4-T045**
Theoretical	8.90	22.05	24.70

3.4 Finite Element Analysis

Commercial software ABAQUS was used to model the characteristic of the sandwich structures under flexural load. The mechanical properties were determined using flexural test for pre-preg carbon fiber and compression test for Nomex honeycomb and X-MP4-T045. The mechanical properties involved in these simulations are elastic and plastic properties for each material. To define the plasticity in Abaqus, true stress, true stain and plasticity equation were used as shown in Eq (3.15).

$$\varepsilon_{pl} = \varepsilon^{t} - \frac{\sigma}{E} \tag{3.15}$$

where

ε_{pl} = plastic strain, mm/mm

ε^{t} = true strain, mm/mm

σ = true stress, MPa

E = Young's modulus, MPa

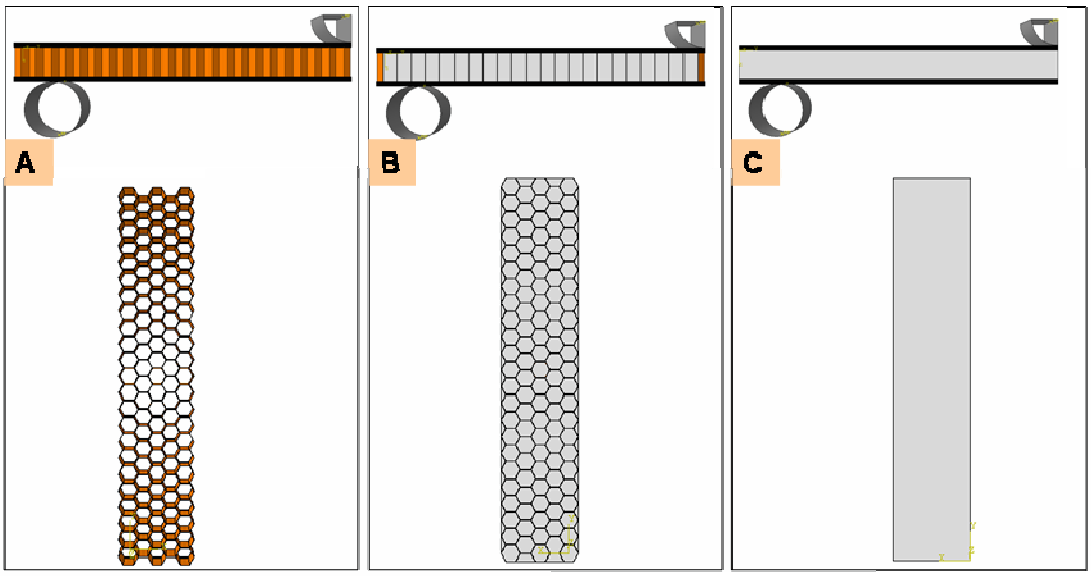

Figure 3.7. ABAQUS model for the three different core materials (A) Honeycomb; (B) H-X-MP4-T045; (C) X-MP4-T045.

One quarter of the samples was simulated because of symmetry as shown in Figure 3.7. The dimension of all the specimens and the fixtures followed exactly the same as experimental conditions. Materials used in this simulation were modeled using solid extractable elements and the loading fixtures were modeled with shell elements with reference points to define the loading and boundary conditions. The displacement was applied at the top of the roller and the displacements at the bottom roller were set to zero.

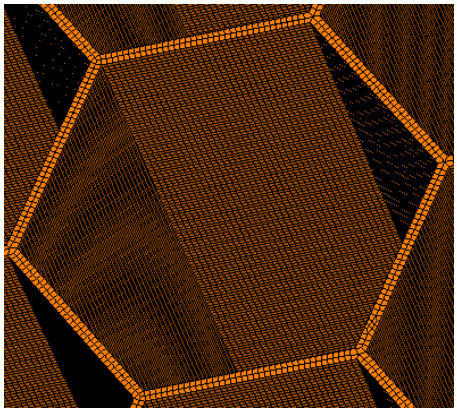

Figure 3.8. Meshing of honeycomb.

Square element meshing method was used in this simulation. Fine mesh was used. 42150 elements used for the face sheets, 18240 elements for X-MP4-T045, 44772 elements for H-X-MP4-T045, and 3304286 for the honeycomb.

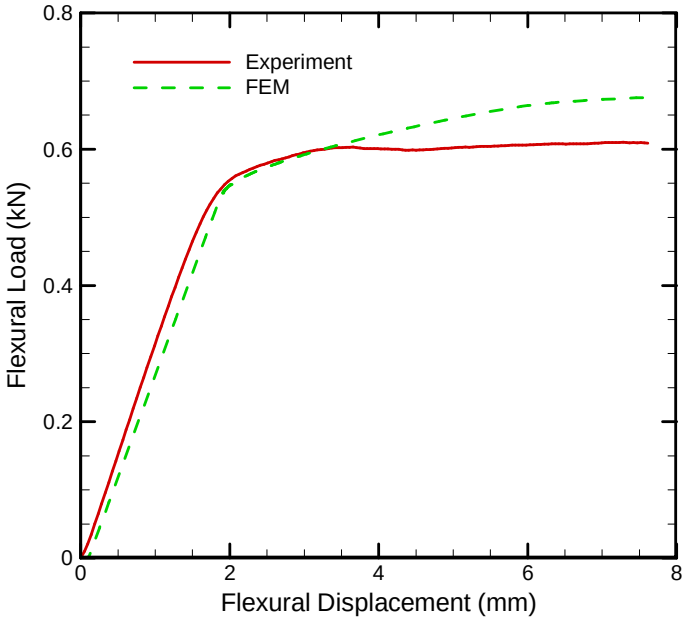

Figure 3.9. Comparison of the load-displacement curve from FEM model and experimental results for honeycomb core.

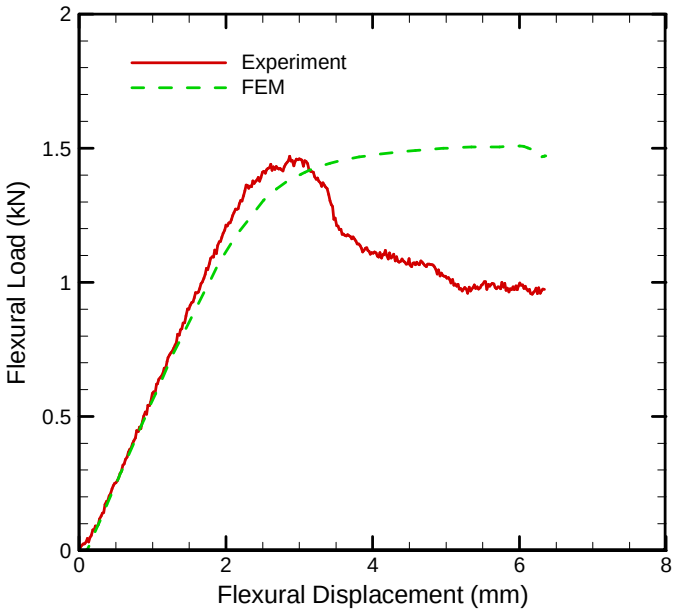

Figure 3.10. Comparison of the load-displacement curve from FEM model and experimental results for H-X-MP4-T045 core.

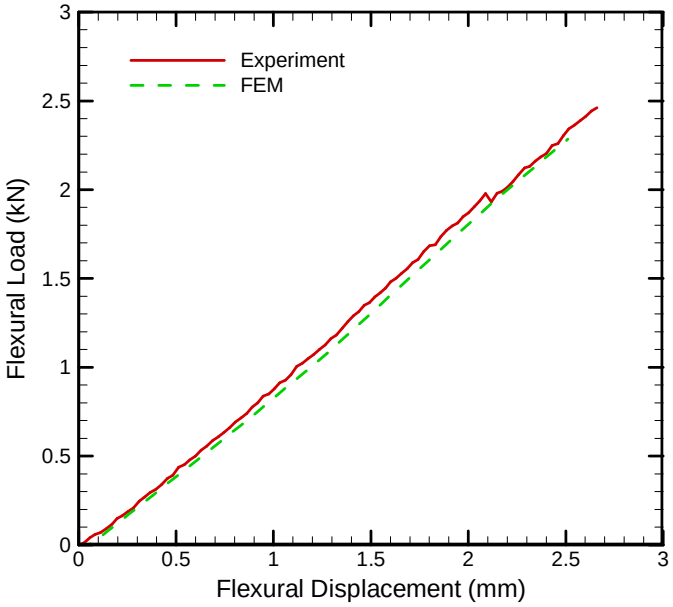

Figure 3.11. Comparison of the load-displacement curve from FEM model and experimental results for X-MP4-T045 core.

Figures 3.10, 3.11 and 3.12 show the comparison between the simulation and experimental results for the sandwiches with the use of three different cores. The results compared favorably for the three composites cores especially in the elastic region. For H-X-MP4-T045 core, the elastic region was almost identical but the plastic region was off by some magnitude. This was because the aerogels inside the hexagonal cell of the honeycomb started to crack at about 2.5 mm as discussed earlier and failure was not modeled in the FEM model.

Table 3.3. Comparison of flexural modulus (GPa) obtained from experiment, theoretical and finite element analysis for honeycomb, H-X-MP4-T045 and X-MP4-T045 cores.

	Honeycomb	**H-X-MP4-T045**	**X-MP4-T045**
Experiment	8.11	14.43	23.12
Theoretical	8.90	22.05	24.70
FEM	7.62	15.69	25.36

The experimental, theoretical and FEM results on the flexural modulus are listed in Table 3.3. Theoretical and FEM analyses were used to predict the experimental results from flexural tests. The results comparison shows a good agreement between the three core materials and only the H-MP4-T045 from the theoretical analysis was off by 35%. The error was related to the Eq. 3.10 which was used to calculate the shear modulus of the core material. The equation was used under the condition that two different constituents were assumed to be perfectly bonded and frictionless. In this study, X-MP4-T045 was only bonded to the face sheets and sliding could occur within the honeycomb

cell. This gives an idea to increase the performance of H-X-MP4-T045 by bonding the crosslinked aerogel with honeycomb.

CHAPTER IV

ACOUSTIC CHARACTERIZATION

4.1 Normal Incidence Sound Absorption Coefficient

The two microphone method using a standing impedance tube was used to measure the normal incidence sound absorption coefficient for the three types of samples. This method is based on ASTM E 1050 standards. The set-up used in this test includes a metal impedance tube, two microphones with two MP-13 Mini-mic preamp, a 1330-B random noise generator made by General Radio Company, a DH200E loud speaker made by Selenium and a Sigma digital oscilloscope made by LDS Nicolet.

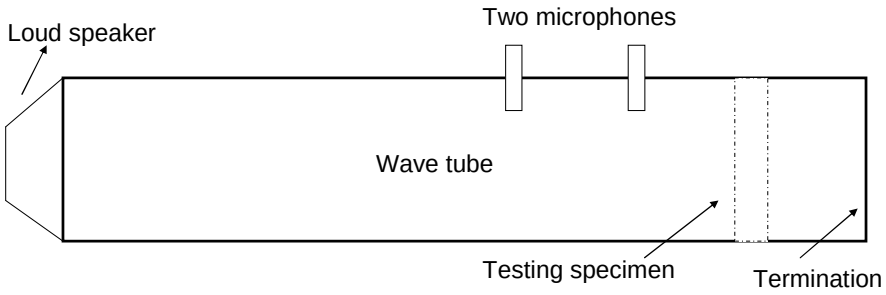

Figure 4.1. Sound absorption coefficient experimental equipments.

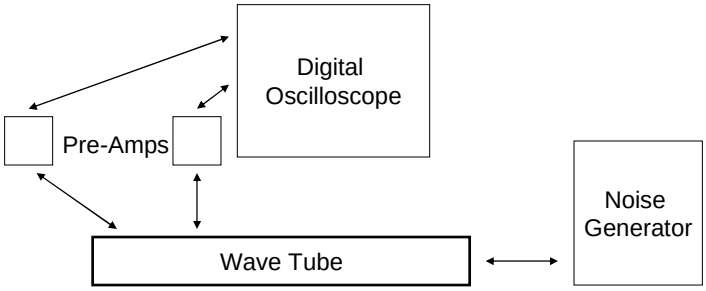

Figure 4.2. A schematic diagram of the two microphones set-up.

The spacing between the two microphones in this set-up is 45 mm which is 80% of the maximum allowable distance which is stated in ASTM E-1050. The two microphones were connected to the top of the impedance tube. The dimensions of the impedance tube are 53.34 mm in diameter and 250 mm in length. The sample size is given in Table 2.1.

4.1.1 Requirement

i) Wave tube

In order to improve the accuracy of the result, a set of requirements must be satisfied. To minimize the effect of sound loss during the test, the impedance tube needs to be constructed with high density material. The connection between the speakers and the sample holders to the impedance tube must be fully sealed to minimize sound loss. The inner surface of the tube must be clean to maintain low sound attenuation.

ii) Working Frequency Range

$$f_L < f < f_U \tag{4.1}$$

where

f = operating frequency, hertz

f_L= lower working frequency of the tube, hertz

f_U= upper working frequency of the tube, hertz

Working frequency range depends on the size of the tube and the spacing of the two microphones. The upper limit frequency is corresponding to the diameter of the impedance tube to maintain plain wave propagation and the limit is defined as

$$f_U < Kc / d \quad or \quad d < Kc / f_U \tag{4.2}$$

where

c = speed of sound, ms^{-1}

d = diameter of the tube, m

K = 0.586

For lower limit frequency, it depends on the spacing of the microphone and the accuracy of the analysis system. A large spacing between the microphones will provide more accurate data. However, the microphones spacing must be less than half wave length of interest.

$$s << c / 2 f_U \tag{4.3}$$

where

s = microphone spacing, m

The recommended maximum microphone spacing is 80% of the $c/2f_U$.

iii) Sound Source

The recommended test signal is random noise with uniform spectral density function. Such spectral line spacing of the test signal must be compatible with the analysis bandwidth. The example of test signal includes pseudo-random noise such as white noise, pink noise, swept sine, and steeped sine.

4.1.2 Calculation

The speed of sound is calculated at the given temperature in the testing environment. The value of the speed of sound is defined as

$$c = 20.47\sqrt{273.15 + T} \tag{4.3}$$

where

c = speed of sound, ms^{-1}

T = temperature in testing environment, °C

The transfer functions are used to calculate the normal incidence sound absorption coefficient. The transfer function is a complex ratio of the acoustic pressure

responses. To avoid any mismatch in the amplitude or phase responses, the calibration between the two microphones is required. The sample used for calibration must be a highly absorptive material. This is to minimize the reflection of sound from the sample back to the microphones. First, the transfer function of the real testing configuration as H^I is measured. Next, the two microphones are interchanged and the transfer function as H^{II} is measured. The calibration transfer function is calculated as follow

$$\overline{H}_c = \left(\overline{H}^I \times \overline{H}^{II}\right)^{1/2} = \left|\overline{H}_c\right| e^{j\bar{\phi}_c} \tag{4.4}$$

$$\left|\overline{H}_c\right| = \left(\left|\overline{H}^I\right| \times \left|\overline{H}^{II}\right|\right)^{1/2} \tag{4.5}$$

$$\phi_c = \frac{1}{2}\left(\bar{\phi}^I + \bar{\phi}^{II}\right) \tag{4.6}$$

Where H is the transfer function, subscript c is calibration, superscript I is first configuration, superscript II is the second configuration and Φ is the phase of the complex transfer function.

The transfer function is calculated by taking the ratio of the cross spectrum density to the input auto power spectrum density function. The equation is defined as

$$\overline{H} = \frac{G_{12}}{G_{11}} = \left|\overline{H}\right| e^{j\bar{\phi}} \tag{4.7}$$

where

H = complex microphone calibration factor

Φ = phase of the complex transfer function

G_{11} = auto spectral density function

G_{12} = cross spectral density function

The transfer function could also be a complex ratio of the Fourier transform of the acoustic pressure of the microphone nearest to the second microphone. The measured transfer function needs to be adjusted with the calibrated transfer function from the highly absorptive specimen as described above. The correct mismatch in the microphone responses is defined as

$$H = \overline{H} / \overline{H}_c = |H| e^{j\bar{\phi}} \tag{4.8}$$

Using the correct mismatch in Eq. 4.8, the final transfer function which was used to calculate the complex reflection coefficient is describe as

$$R = |R| e^{j\phi R} = \frac{H - e^{-jks}}{e^{jks} - H} e^{j2k(l+s)} \tag{4.9}$$

$$k = 2\Pi f / c \tag{4.10}$$

where

R = complex reflection coefficient

H = transfer function with mismatch corrected

k = wave number, m^{-1}

l = distance from the test sample to the center of the nearest microphone, m

s = spacing between the microphones, m

f = frequency, s^{-1}

Finally the normal incidence sound absorption coefficient as follows

$$\alpha = 1 - |R|^2 \tag{4.11}$$

where

α = sound absorption coefficient

R = complex reflection coefficient

4.1.3 Results and Discussions

Sixteen averages were taken from the two samples for each core materials. To minimize the environmental noise effect, sound source of 10 db higher than the environmental noise was used.

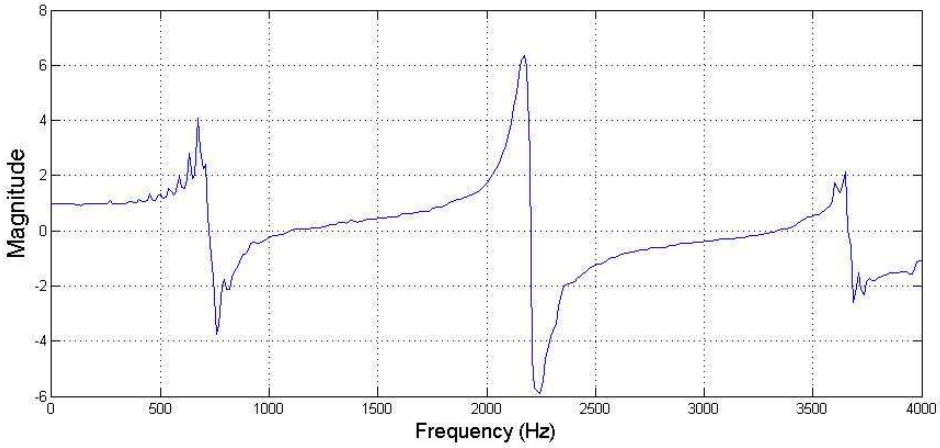

Figure 4.3. Plot of transfer function for honeycomb core.

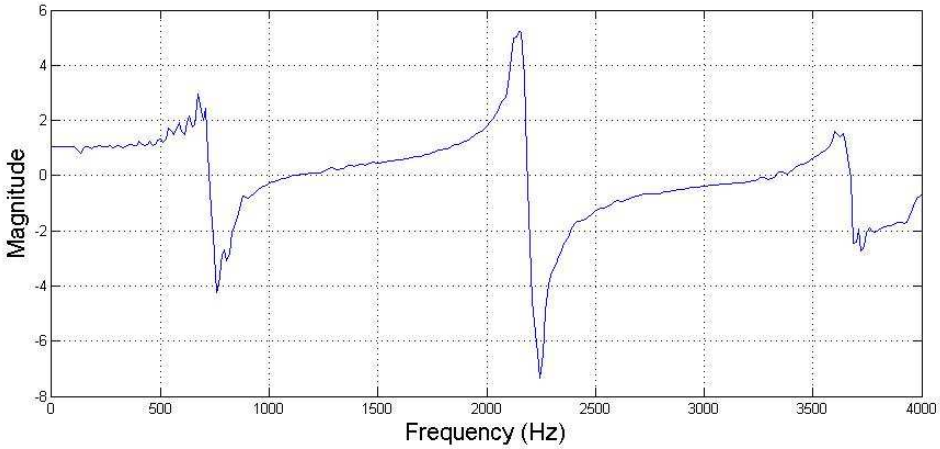

Figure 4.4. Plot of transfer function for H-X-MP4-T045.

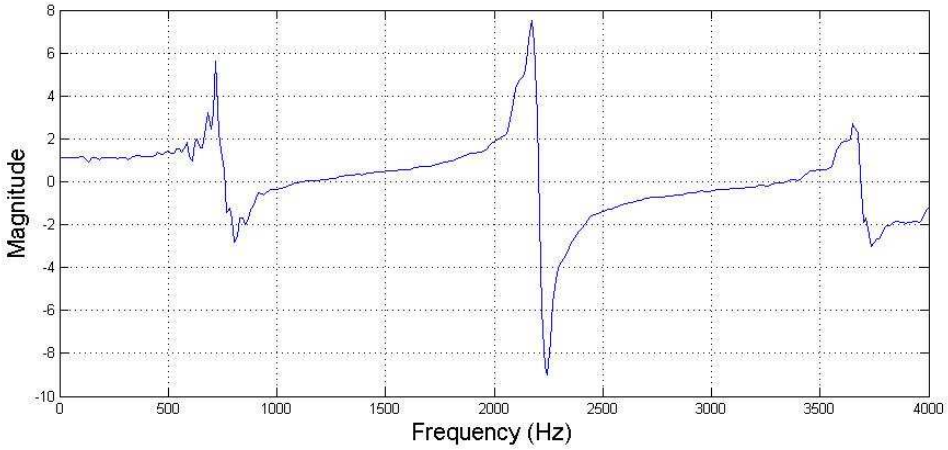

Figure 4.5. Plot of transfer function for X-MP4-T045.

Figures 4.3, 4.4 and 4.5 show the transfer function for honeycomb, H-X-MP4-T045 and X-MP4-T045 cores. The variations between the three plots are not much and the characteristic of heavier material is higher than lighter material as can be seen. The order of heavier to lighter sample is X-MP4-T045, H-X-MP4-T045 and honeycomb. There is some fluctuation in the low frequency range and this indicates that the result is not accurate at the point. The results might be affected by the vibration from the speaker to the wave tube, the low frequency environmental noise and also the limitation of the tube dimension. The accuracy was believed to be in between 315 Hz and 4000 Hz and all of the results will only be reported in this range.

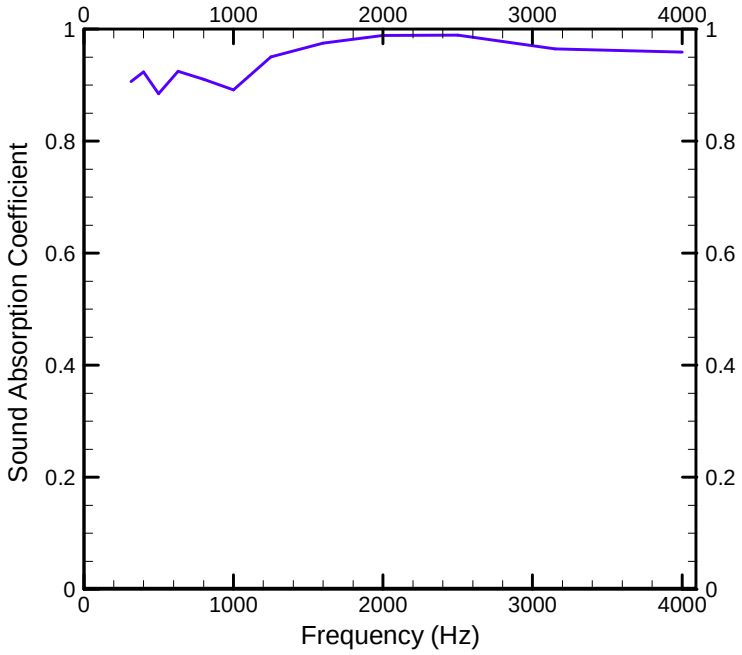

Figure 4.6. Preliminary test of highly absorptive material.

Figure 4.6 shows the results of a highly absorptive material which was also used in the calibration as discussed in section 4.1.2. Sponge of thickness approximately 10 mm

was used as the preliminary sample to test the accuracy of the set-up. The sound absorption coefficient has a value range from 0 to 1 with 0 representing highly reflective, and 1 representing highly absorptive. The results agree with the characteristic of the sponge material very well with the results almost close to 1.

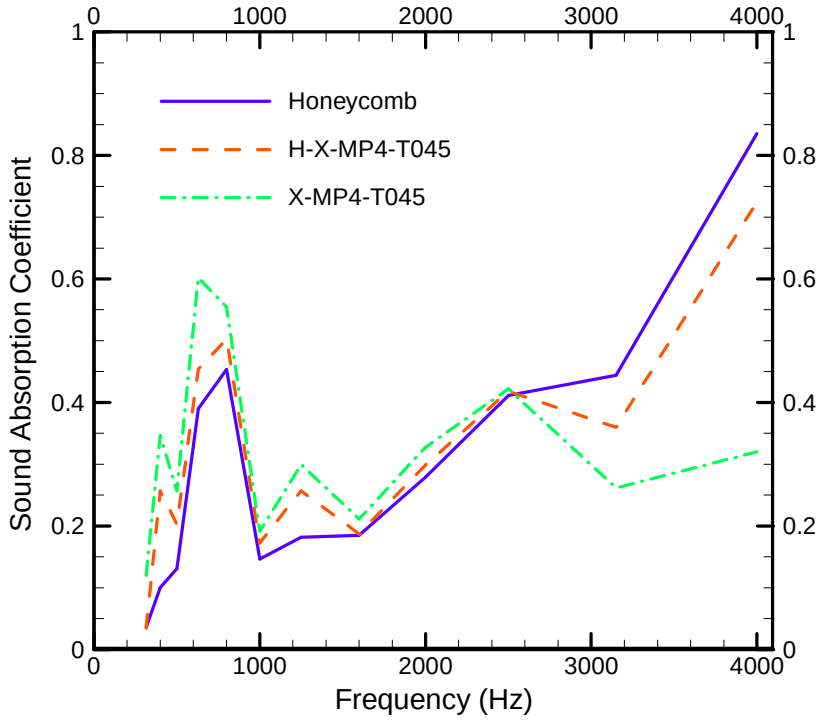

Figure 4.7. Plot of sound absorption coefficient.

Figure 4.7 shows the results of the sound absorption coefficient of the three core materials. Two samples were used for each specimen and each test was repeated 4 times and the results were averaged. The variation between the three specimens only occurs at low frequency and high frequency. At the mid range frequency, the results of the three core materials almost converge. Also, at low frequency, X-MP4-T045 absorbed more

sound than the other two. At higher frequency, honeycomb core performed better than the X-MP4-T045, and H-X-MP4-T045 was close to honeycomb core.

4.2 Sound Transmission Loss

The measurement of normal incidence transmission loss is the extension of the measurement of the normal incidence sound absorption coefficient. Almost all testing standard used to measure sound transmission loss involved a large chamber and a sample size close to the service condition. A new method was published in 2006 with the use of a small wave tube, 4 microphones, noise generator and a FFT analyzer [1]. As reported, the accuracy of this test is as high as 95% when compared to the ASTM E-1289 when the correct dimensions of the impedance tube are used.

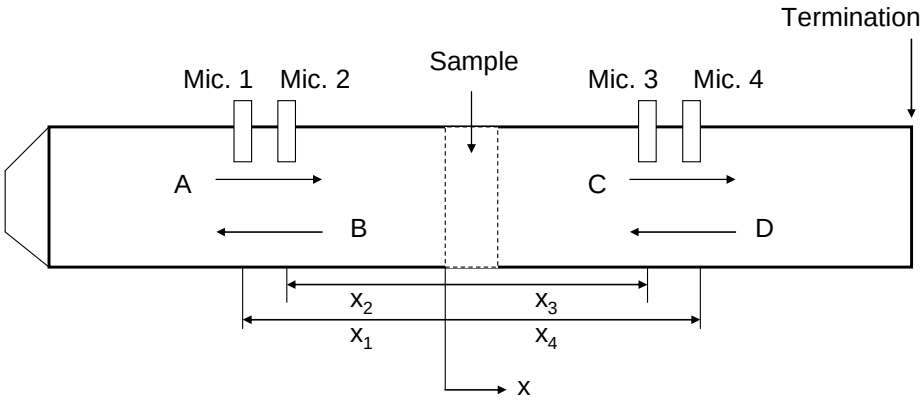

Figure 4.8. Sound transmission loss experimental equipment.

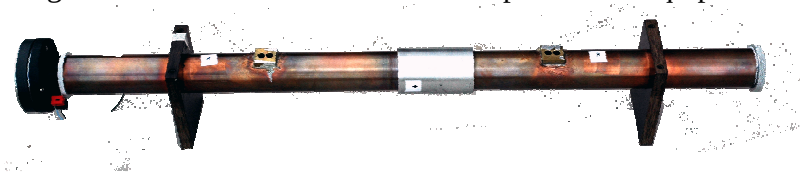

Figure 4.9. Metal impedance tube with 53.34 mm inner diameter.

The length of the impedance used in this test is two times longer than the impedance tube used to determine sound absorption. Also, two more microphones were added to the other sides of the impedance tube to detect the acoustic signals after it has passed through the samples. These signals were used to calculate the normal incidence transmission loss. The dimension requirement was the same as described in Section 4.1.1 and the set-up includes a noise generator, four pre-amps, a loud speaker and an oscilloscope which were described in 4.1. The spacing of the microphones was reduced to 11 mm between microphone 1 and 2 in the first section and microphone 3 and 4 in the second section of the impedance tube.

4.2.1 Calculations

If the requirement of the distance between the sound source and the first microphone was met at frequencies below the cutoff frequency, only plane waves can propagate in the tube. In this case, the sound pressure and velocity are described as follows

$$p(x,t) = \mathrm{Re}\left\{P(x,\omega)e^{j\omega t}\right\} = \begin{cases} \mathrm{Re}\left\{\left(A(\omega)e^{-jkx} + B(\omega)e^{jkx}\right)e^{j\omega t}\right\} & x \le 0 \\ \mathrm{Re}\left\{\left(C(\omega)e^{-jkx} + D(\omega)e^{jkx}\right)e^{j\omega t}\right\} & x \ge l \end{cases}$$

$$v(x,t) = \mathrm{Re}\left\{V(x,\omega)e^{j\omega t}\right\} = \begin{cases} \mathrm{Re}\left\{\dfrac{\left(A(\omega)e^{-jkx} + B(\omega)e^{jkx}\right)}{\rho_0 c}e^{j\omega t}\right\} & x \le 0 \\ \mathrm{Re}\left\{\dfrac{\left(C(\omega)e^{-jkx} + D(\omega)e^{jkx}\right)}{\rho_0 c}e^{j\omega t}\right\} & x \ge l \end{cases} \quad (4.12)$$

where

Re{} = the real part of

P = complex pressure

V = complex particle velocity

A to D = complex amplitudes of the plane wave components

ρ_0 = ambient fluid density, kgm^{-3}

c = ambient sound speed, ms^{-1}

ω= angular frequency, s^{-1}

k = wave number, m^{-1}

l = thickness of sample, m

Eq. 4.12 can be expressed in terms of complex pressure P_1 to P_4 at position x_1 to x_4 as shown in Figure 4.8

$$A = \frac{j\left(P_1 e^{jkx_2} - P_2 e^{jkx_1}\right)}{2\sin k\left(x_1 - x_2\right)} \qquad C = \frac{j\left(P_3 e^{jkx_4} - P_4 e^{jkx_3}\right)}{2\sin k\left(x_3 - x_4\right)}$$
$$B = \frac{j\left(P_2 e^{-jkx_1} - P_1 e^{-jkx_2}\right)}{2\sin k\left(x_1 - x_2\right)} \qquad D = \frac{j\left(P_4 e^{-jkx_3} - P_3 e^{-jkx_4}\right)}{2\sin k\left(x_3 - x_4\right)} \tag{4.13}$$

The complex acoustic pressure can be replaced by the transfer function with microphone 1 as the reference signal.

$$A = \frac{j\left(H_{P_1R} e^{jkx_2} - P_2 e^{jkx_1}\right)}{2\sin k\left(x_1 - x_2\right)} \qquad C = \frac{j\left(H_{P_3R} e^{jkx_4} - P_4 e^{jkx_3}\right)}{2\sin k\left(x_3 - x_4\right)}$$
$$B = \frac{j\left(H_{P_2R} e^{-jkx_1} - P_1 e^{-jkx_2}\right)}{2\sin k\left(x_1 - x_2\right)} \qquad D = \frac{j\left(H_{P_4R} e^{-jkx_3} - P_3 e^{-jkx_4}\right)}{2\sin k\left(x_3 - x_4\right)} \tag{4.14}$$

The transfer function can be expressed as the ratio of the auto-spectral density function at microphone location 1 to 4 to the cross-spectral density function of the reference signal at 1 to 4 to the reference signal which is at 1.

$$H_{P_iR}(f) = G_{RP_i}(f) / G_{RR}(f) \tag{4.15}$$

The transfer matrix can be used to relate the pressure and velocity in the first section of the tube and the pressure and velocity in the second section of the tube in figure 4.8.

$$\begin{bmatrix} P \\ V \end{bmatrix}_{x=0} = \begin{bmatrix} T_{11} & T_{12} \\ T_{21} & T_{22} \end{bmatrix} \begin{bmatrix} P \\ V \end{bmatrix}_{x=d} \tag{4.16}$$

Eq. 4.16 involved two equations but with four unknowns. In order to determine the unknowns, a second termination condition is added to Eq. 4.17

$$\begin{bmatrix} P^{(a)} & P^{(b)} \\ V^{(a)} & V^{(b)} \end{bmatrix}_{x=0} = \begin{bmatrix} T_{11} & T_{12} \\ T_{21} & T_{22} \end{bmatrix} \begin{bmatrix} P^{(a)} & P^{(b)} \\ V^{(a)} & V^{(b)} \end{bmatrix}_{x=d} \tag{4.17}$$

where a and b represent the two termination conditions (open and close). By inverting the matrix expression, the four unknowns are expressed as

$$\begin{bmatrix} T_{11} & T_{12} \\ T_{21} & T_{22} \end{bmatrix} = \tag{4.18}$$

$$\frac{\begin{bmatrix} P^{(a)}\big|_{x=0} V^{(b)}\big|_{x=d} - P^{(b)}\big|_{x=0} V^{(a)}\big|_{x=d} & - P^{(a)}\big|_{x=0} P^{(b)}\big|_{x=d} + P^{(b)}\big|_{x=0} P^{(a)}\big|_{x=d} \\ V^{(a)}\big|_{x=0} V^{(b)}\big|_{x=d} - V^{(b)}\big|_{x=0} V^{(a)}\big|_{x=d} & - P^{(b)}\big|_{x=d} V^{(a)}\big|_{x=0} + P^{(a)}\big|_{x=d} V^{(b)}\big|_{x=0} \end{bmatrix}}{P^{(a)}\big|_{x=d} V^{(b)}\big|_{x=d} - P^{(b)}\big|_{x=d} V^{(a)}\big|_{x=d}}$$

The pressures and the velocities may be expressed in terms of coefficient A to D from the transfer function.

$$P^{(s)}\Big|_{x=0} = A^{(s)} + B^{(s)}, \quad P^{(s)}\Big|_{x=d} = C^{(s)}e^{-jkd} + D^{(s)}e^{jkd},$$
$$V^{(s)}\Big|_{x=0} = \frac{A^{(s)} - B^{(s)}}{\rho_0 c}, \quad V^{(s)}\Big|_{x=d} = \frac{C^{(s)}e^{-jkd} - D^{(s)}e^{jkd}}{\rho_0 c} \tag{4.19}$$

After substituting Eq. 4.19 into Eq. 4.18, the four unknowns can be used to calculate the normal incidence sound transmission loss. With a perfectly anechoic termination which the coefficient D=0, the sound transmission loss is

$$TL_n(\omega) = 10 \log\left(\frac{1}{4}\left|T_{11} + \frac{T_{12}}{\rho_0 c} + \rho_0 c T_{21} + T_{22}\right|^2\right) \tag{4.20}$$

4.2.2 Results and Discussion

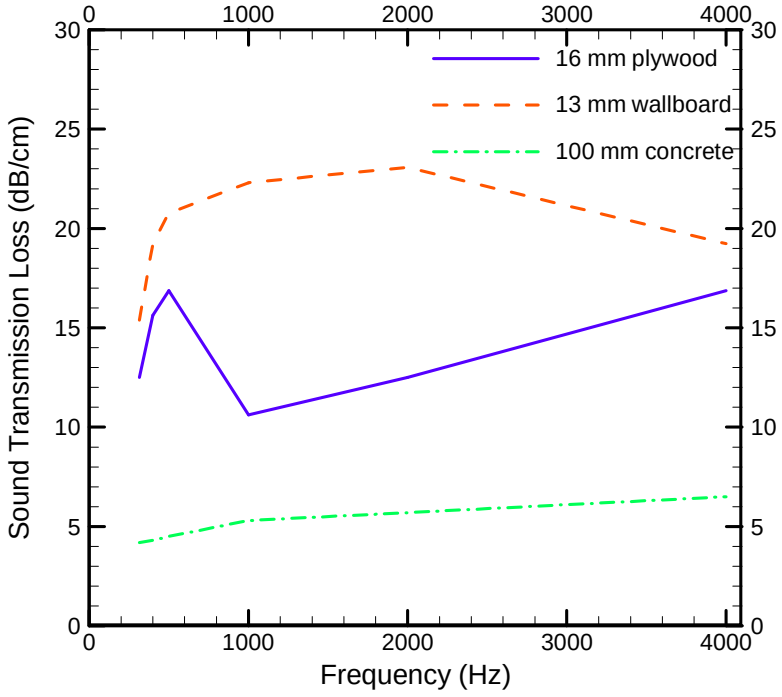

Figure 4.10. Plot of sound transmission loss for common wall material [7].

Figure 4.10 shows the sound transmission loss of common wall material with the data taken from National Research Council Canada [7]. In order to get a comparison with the sandwich structures used in this study, the sound transmission loss was normalized by dividing the thickness of the samples. The results for homogenous material can be predicted easily and the equation is derived as

$$TL = 20 \log(mf) - 47 \tag{4.21}$$

where

TL = sound transmission loss, dB

m = mass per unit area, kgm^{-2}

f = frequency, Hz

For non homogenous material such as sandwich structure, the calculation involved the configuration of all the materials. If designed correctly, the sound transmission loss can be better than homogenous material and also it gives lower density.

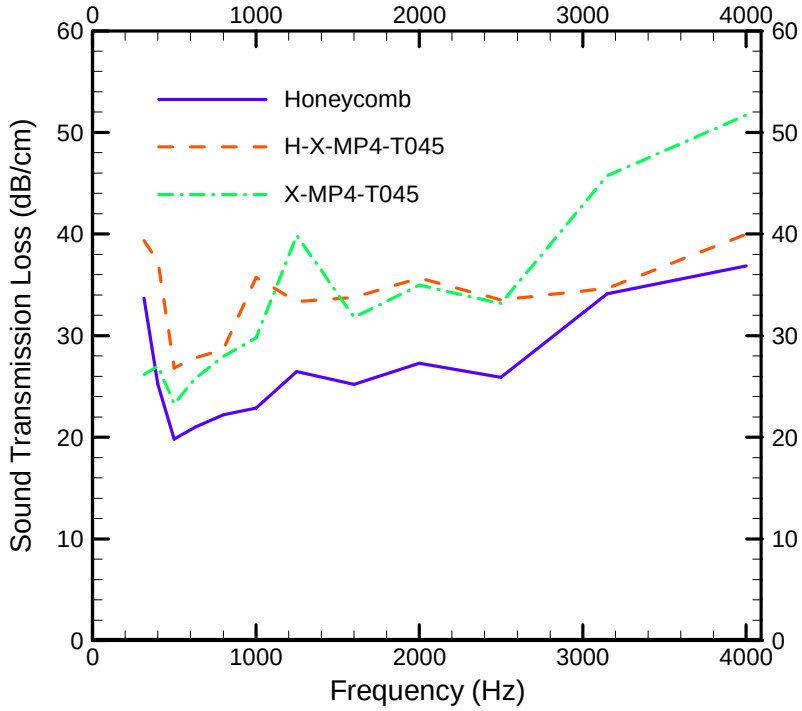

Figure 4.11. Plot of sound transmission loss.

To minimize the error, sixteen averages data were taken from the two samples for the three core materials. The results showed that there is only little variation between the

there core materials at low frequency. However, H-X-MP4-T045 and H-X-MP4-T045 substantially performed better than honeycomb core especially in the range between1000 Hz and 3000 Hz. The results also showed that H-X-MP4-T045 and X-MP4-T045 were close to each other until 3000 Hz. The X-MP4-T045 core composite gives 12 dB higher transmission loss at 4000 Hz. X-MP4-T045 and H-X-MP4-T045 composites have higher sound transmission loss at all the frequency range.

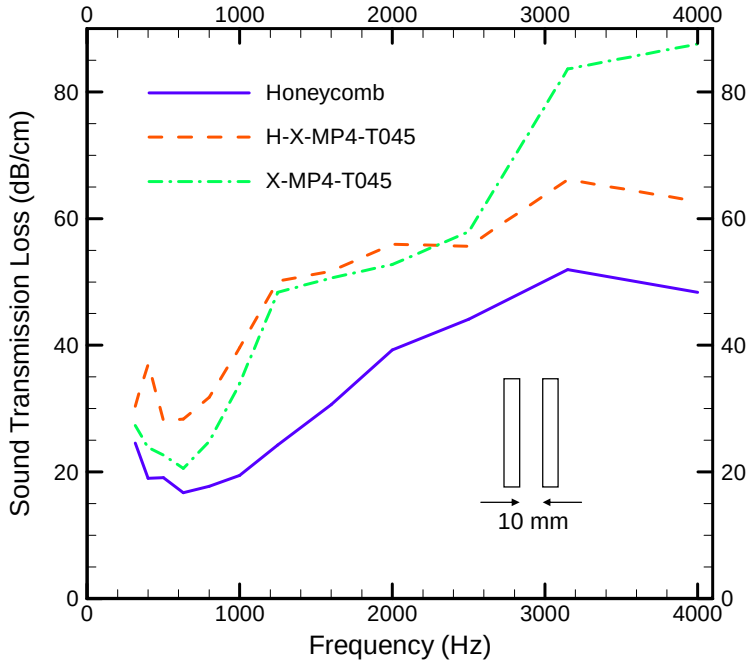

Figure 4.12. Plot of sound transmission loss of two layer specimens with 10 mm air gap.

Two layers could be used to enhance the performance of sound insulation. When two layers are bonded perfectly together, it behaves like a single thick layer with an associated lowering of the coincidence frequency. However, when the two layers are only held together loosely, the friction between the layers can introduce some energy losses

[7]. Another idea is to separate the two layers by some distance leaving an air gap or placing the gap by some absorptive material, if designed correctly, it can highly improve sound transmission loss [8]. In Figure 4.12, two layers of composites were used, with 10 mm air gap between. As can be seen, the sound transmission loss of the three core materials was increased by some amount with H-X-MP4-T045 and X-MP4-T045 reached 63 dB and 87 dB at 4000 Hz, respectively.

CHAPTER V

CONCLUSION

5.1 Conclusion

Crosslinked aerogel with crosslinker N3200, X-MP4-T045 was fabricated and to determine their mechanical property and acoustic transmission loss. The crosslinked aerogel was used as the primary core material and also used to embed into Nomex Honeycomb for use as core material in a composite sandwich beam. The expectations of these types of light weight core materials were to provide advantages in mechanical strength and acoustic insulation.

Three type of core materials were tested follow ASTM D 790 standards. There core materials are honeycomb, honeycomb embedded crosslinked aerogel, X-MP4-T045 and crosslinked aerogel, X-MP4-T045. It was shown that X-MP4-T045 is excellent in resisting bending stress and has the highest ultimate strength and flexural modulus. However, brittle failure mode was occurred at 0.008 flexural strain for X-MP4-T045 core. For H-X-MP4-T045, the density increased by 35% but the flexural modulus and the ultimate strength increased by 40% and 46.84%, respectively when compared to the honeycomb core. The honeycomb core is favor in flexibility but has the lowest flexural

strength and modulus. The theoretical and numerical results matched very well with the experimental results.

The specimens were also tested for the performance of acoustic insulation. The acoustic tests involved sound absorption coefficient and sound transmission loss both serve as important criteria of acoustic insulation. It was shown that honeycomb core absorbed more sound at higher frequency but was little disadvantage at lower frequency. For sound transmission loss, X-MP4-T045 showed highest performance and the results for H-X-MP4-T045 was close to X-MP4-T045 except at higher frequency. Two samples with 10 mm air gap in between were tested and the results were highly enhanced. These results were compared to commercial wall material using normalization by dividing the sound transmission loss to the wall thickness. The results showed that X-MP4-T045 and H-X-MP4-T045 core performed better.

CHAPTER VI

FUTURE WORK

The crosslinked aerogel core composites are intended for multifunctional applications. The following work is suggested for future work.

Thermal Insulation Test

The crosslinked aerogel core composites can be tested to determine their conductivity. The material can be formulated so that it will combine optimal thermal conductivity with high mechanical strength and high acoustic damping.

Impact Test

Crosslinked aerogels have been determined to have high energy absorption capability. Further evaluation is suggested to determine the energy absorption under dynamic loading. In this area, high velocity impact test can be conducted for a crosslined aerogel core sandwich structure with the use of three different core materials for comparison. The drop-weight test is suggested to be conducted with the velocity measured before and after impact to calculate the energy absorption for comparison.

Materials

Different types of crosslinked aerogels can be formulated and to embed into the Nomex honeycomb core to evaluate its multifunctional performance in comparison with the previous X-MP4-T045 core. For example, a low density polyurea crosslinked aerogels have been recently made. Polyurea crosslinked aerogels could become a good candidate material for further investigation.

REFERENCES

[1] O. Olivieri, J. Stuart Bolton, T. Yoo, “Measurement of transmission loss of materials using a standing wave tube”, INTER-NOISE 2006.

[2] N. Leventis, S. Mulik, X. Wang, A. Dass, V. U. Patil, C. Sotirious-Leventis, H. Lu, G. Churu, A. Capecelatro, “Polymer nano-encapsulation of templated mesoporous silica monoliths with improved mechanical properties”, Journal of Non-Crystalline Solids, 354, 632-344, 2008.

[3] G. Zhang, A. Dass, A. M. Rawashdeh, J. Thomas, J. A. Counsil, C. Sotiriou-Leventis, E. F. Fabrizio, F. I., J. C. Johnson, M. A. Meador, N. Leventis, “Isocyanate-crosslinked silica aerogel monolith : preparation and characterization”, Journal of Non-Crystalline Solids, 350, 152-164, 2004.

[4] L. A. Capadona, M. A. B. Meador, A. Alunni, E. F. Fabrizio, P. Vassilaras, N. Leventis, “Flexible, low density polymer crosslinked silica aerogels”, Polymer 47, 5754-5761, 2006.

[5] M. Schmidt, F. Schwertfeger, “Applications for silica aerogel products”, Journal of Non-Crystalline Solids, 225, 364-368, 1998.

[6] Sandwich concept, DIAB sandwich handbook. Available from: www.diabgroup.com.

[7] A.C.C. Warnock. CBD-239 Factors Affecting Sound Transmission Loss. National Research Council Canada 1985.

[8] L. Forest, V. Gibiat, T. Woignier, “Biot’s theory of acoustic propagation in porous media applied to aerogels and alcogels, Journal of Non-Crystalline Solids 225, 287-292, 1998.

[9] L. D. Gelb, “Simulating Silica Aerogels with a Coarse-Grained Flexible Model and Langevin Dynamics”, J. Phys. Chem. C, 111, 15792-15802, 2007.

[10] A.H. Sheikh, P.H. Bull, J.A. Kepler, “Behaviour of multiple composite plates subjected to ballistic impact”, Composites Science and Technology 69, 704-710, 2009.

[11] N. Gupta, W. Ricci, “Processing and compressive properties of aerogel/epoxy composites”, Journal of Materials Processing Technology 198, 178-182, 2008.

[12] A. A. Anappara, S. Rajeshkumar, P. Mukundan, P.R.S. Warrier, S.Ghosh, K.G.K. Warrier, “Impedance spectroscopic studies of sol-gel derived subcritically dried silica aerogels”, Acta Materialia, 52, 369-375, 2004.

[13] C. Foo, G. Chai, L. Seah, “Mechanical properties of Nomex material and Nomex honeycomb structure”, Composite Structures, 80, 588-594, 2007.

[14] M. Styles, P. Compston, S. Kalyanasundaram, “The effect of core thickness on the flexural behaviour of aluminum foam sandwich structures”, Composite Structures, 80, 532-538, 2007.

[15] H. Bart-Smith, J.W. Hutchinson, A.G. Evans, “Measurement and analysis of the structural performance of cellular metal sandwich construction”, International Journal of Mechanical Sciences, 43, 1945-1963, 2001.

[16] C. A. Steeves, N. A. Fleck, “ Collapse mechanisms of sandwich beams with composite faces and a foam core, loaded in three-point bending. Part I: analytical models

and minimum weight design", International Journal of Mechanical Sciences, 46, 561-583, 2004.

[17] M. Styles, P. Compston, S. Kalyanasundaram, " Finite element modeling of core thickness effects in aluminum foam/composite sandwich structures under flexural loading", Composite Structures, 86, 227-232, 2008.

[18] J. Fricke, 1992. Aerogels and their applications. Journal of Non-Crystalline Solids 147&148 356-362.

[19] L. Gibson, M. Ashby., 1997. Cellular Solids: Structure and Properties, 2nd Edition, Cambridge University Press.

[20] B. Good., 2006. Computer simulation of fracture in aerogels. In: Material Research Society Symposium Proceeding.

[21] S. Jones,2006.Aerogel: Space exploration applications. Journal of Sol-Gel Science and Technology 40, 351-357.

[22] N. Leventis, C. Sotiriou-Leventis, C. Zhang, G. Rawashdeh, 2002. Nanoengineering strong silica aerogels. Nano letters 2(9) 957-960.

[23] N. Leventis, 2007. Three-dimensional core-shell superstuctures: mechanically strong aerogels. Accounts of Chemical Research 40 874-884.

[24] N. Leventis, S. Mulik, X. Wang, A. Dass, C. Sotiriou-Leventis, H. Lu, 2007. Stresses at the interface of micro with nano. Journal of the American Chemical Society 129 10660-10661.

[25] H. Luo, H. Lu, N. Leventis, 2006. The compressive behavior of isocyanate-crosslinked silica aerogel at high strain rates. Mechanics Time-Dependent Materials 10 83-111.

[26] H. Luo, G. Churu, E. Fabrizio, J. Schnobrich, A. Hobbs, A. Dass, S. Mulik, Y. Zhang, B. Grady, A. Capecelatro, C. Sotiriou-Leventis, H. Lu, N. Leventis, 2008. Synthesis and Characterization of the Physical. Chemical and Mechanical Properties of Isocyanate-Crosslinked Vanadia Aerogels. Journal of Sol-Gel Science and Technology 48 113-134.

[27] T. Woigner, J. Phalippou, 1989. Scaling law variation of the mechanical properties of silica aerogels. Revue De Physique Appliquee C4-179-184.

[28] T. Woignier, J. Pelous, J. Phalippou, R. Vacher, E. Courtens, 1987. Elastic properties of silica aerogels. Journal of Non-Crystalline Solids 95&96 1197-1202.

APPENDICES

A.1 Material Properties

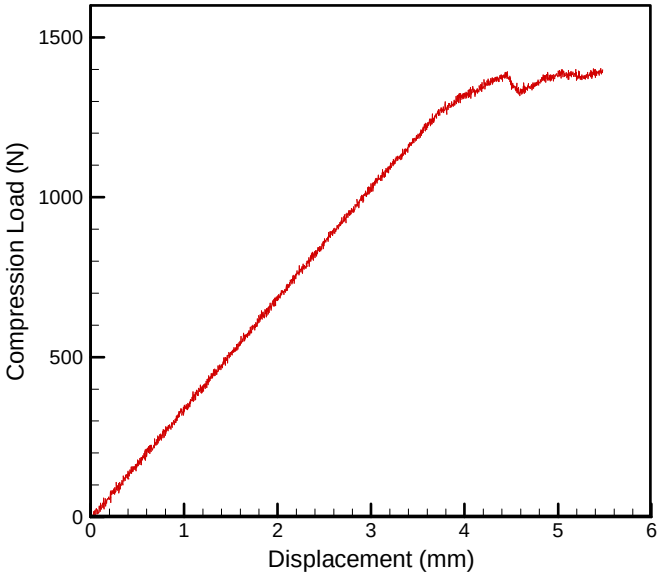

Figure A.1. Flexural data for pre-preg carbon fiber

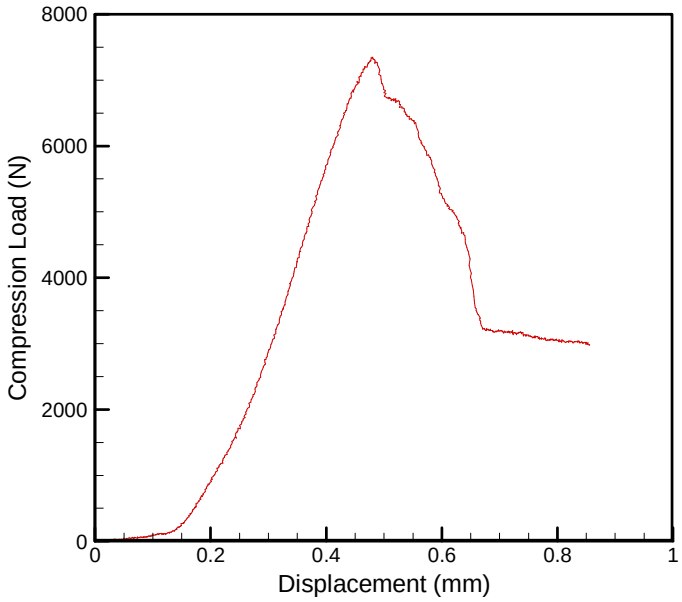

Figure A.2. Compression data for honeycomb

A.2 Matlab Code

Sound Absorption Coefficient

```
j=sqrt(-1);
L=length(Ia);
nfft=2^nextpow2(L);
%% one11 and one22 are the testing microphone calibration
[h1,f]=tfestimate(one11,one22,[],[],nfft/2+1,1/5e-6);
%% two11 and two22 are after switching posiiton
h2=tfestimate(two11,two22,[],[],nfft/2+1,1/5e-6);
%% hc is the calibration transfer function
hc=(h1.*h2).^0.5;
[h,F]=tfestimate(Ia,Ib,[],[],nfft/2+1,1/5e-6);
%% the final transfer function corrected by the calibration factor
H=(h./hc)
```

```
%% calculation of angular frequency
W=2*pi*F/344.989;
%% calculation of sound reflection coefficient
r=((H-exp(-j*W*0.045))./(exp(j*W*0.045)-H)).*(exp(j*2*W*(0.12)));

%% calculation of sound absorption coefficient
alpha=1-(real(r)).^2-(imag(r)).^2;
```

Sound Transmission Loss

```
%% Ia four microhphone data from first termination condition
%% Ib four microphone data from second termination condition
function Output=TB4(Ia,Ib)
%%Constant value of some input variables
x1=-0.2175;
x2=-0.2065;
x3=0.1775;
x4=0.1885;
d=0.05334;
c=344.989;
R=1.21;
f=1/5e-6;
L=length(Ia(:,1));
nfft=2^nextpow2(L);

%%Calculate the transfer function
for i=1:4
[Ha(:,i),Output(:,1)]=tfestimate(Ia(:,1),Ia(:,i),[],[],nfft/2+1,f);
Hb(:,i)=tfestimate(Ib(:,1),Ib(:,i),[],[],nfft/2+1,f);
```

```
end
%% Calculate Complex amplitudes of the plane wave components
k=2*pi.*Output(:,1)/c;
Aa=j*(Ha(:,1).*exp(j*k*x2)-Ha(:,2).*exp(j*k.*x1))./(2*(sin(k*(x1-x2))));
Ba=j*(Ha(:,2).*exp(-j*k*x1)-Ha(:,1).*exp(-j*k.*x2))./(2*(sin(k*(x1-
x2))));
Ca=j*(Ha(:,3).*exp(j*k*x4)-Ha(:,4).*exp(j*k*x3))./(2*(sin(k*(x3-x4))));
Da=j*(Ha(:,4).*exp(-j*k*x3)-Ha(:,3).*exp(-j*k*x4))./(2*(sin(k*(x3-
x4))));

Ab=j*(Hb(:,1).*exp(j*k*x2)-Hb(:,2).*exp(j*k*x1))./(2*(sin(k*(x1-x2))));
Bb=j*(Hb(:,2).*exp(-j*k*x1)-Hb(:,1).*exp(-j*k*x2))./(2*(sin(k*(x1-
x2))));
Cb=j*(Hb(:,3).*exp(j*k*x4)-Hb(:,4).*exp(j*k*x3))./(2*(sin(k*(x3-x4))));
Db=j*(Hb(:,4).*exp(-j*k*x3)-Hb(:,3).*exp(-j*k*x4))./(2*(sin(k*(x3-
x4))));
%% Calculate the pressures and particle velocities
Pa0=(Aa+Ba);
Pad=(Ca.*exp(-j*k*d)+Da.*exp(j*k*d));
Va0=((Aa-Ba)/R/c);
Vad=((Ca.*exp(-j*k*d)-Da.*exp(j*k*d))/R/c);

Pb0=(Ab+Bb);
Pbd=(Cb.*exp(-j*k(:,1).*d)+Db.*exp(j*k(:,1).*d));
Vb0=((Ab-Bb)./R./c);
Vbd=((Cb.*exp(-j*k(:,1)*d)-Db.*exp(j*k(:,1)*d))./R./c);

%% Calculate frequency dependent quantities Tij.
```

```
T11=(Pa0.*Vbd-Pb0.*Vad)./(Pad.*Vbd-Pbd.*Vad);
T12=(-Pa0.*Pbd+Pb0.*Pad)./(Pad.*Vbd-Pbd.*Vad);
T21=(Va0.*Vbd-Vb0.*Vad)./(Pad.*Vbd-Pbd.*Vad);
T22=(-Pbd.*Va0+Pad.*Vb0)./(Pad.*Vbd-Pbd.*Vad);

%% Calculate sound tranmission loss
Output(:,2)=10*log10(0.25*(abs((T11+T12/R/c+R*c*T21+T22)).^2));
end
```

VITA

KahKit Chan

Candidate for the Degree of

Master of Science

Thesis: POLYMER NANOENCAPSULATED SURFACTANT TEMPLATED AEROGEL CORE COMPOSITES FOR MULTIFUNCTIONAL APPLICATION

Major Field: Mechanical Engineering

Biographical:

Personal Data:
Born in Ipoh, Malaysia on Feb. 08, 1983, son of SiewChong Chan and YewLian Choong

Education:
Received Bachelor of Science degree in Mechanical Engineering from Oklahoma State University in May, 2006.
Completed the requirements for the Master of Science in Mechanical Engineering at Oklahoma State University, Stillwater, Oklahoma in July, 2009.

Experience:
Research Assistant**,** 01/2007-present, Polymer Mechanics Laboratory, Oklahoma State University

Name: KahKit Chan Date of Degree: July, 2009

Institution: Oklahoma State University Location: Stillwater, Oklahoma

Title of Study: POLYMER NANOENCAPSULATED SURFACTANT TEMPLATED AEROGEL CORE COMPOSITES FOR MULTIFUNCTIONAL APPLICATION

Pages in Study: 65 Candidate for the Degree of Master of Science

Major Field: Mechanical Engineering

Scope and Method of Study:
In this work, processes are developed to prepare crosslinked aerogel composite sandwich structure to provide multifunctionality. The crosslinked aerogel sandwich structures will be characterized to determine their acoustic and mechanical properties. The sound absorption coefficient and sound transmission loss are measured by an impedance tube, with the use of two and four microphones set-up, an oscilloscope and a noise generator. For mechanical testing, flexural test (ASTM D-790) was used to evaluate the strength and stiffness of crosslinked aerogel composite structure in three point bending. The results are compared with conventional Nomex core composites. Experimental data are compared with analytical and numerical results.

Findings and Conclusions:
Results showed that when light weight crosslinked aerogel was used as a core material in a sandwich structures, the sound insulation was enhanced when compared to conventional Nomex honeycomb core. It was also shown that when crosslinked aerogel were embedded into honeycomb, the performance of sound insulation was close to crosslinked aerogel core with density lowered by 12%. The sound transmission loss was compared favorably with some common insulation materials. Mechanical testing showed great improvement in flexural modulus and strength for crosslinked aerogel core but brittle failure mode was occurred at 0.8 flexural strain. For crosslinked aerogel embedded into Nomex honeycomb, the flexural modulus and strength were lowered by 37.5% and 44.6%, respectively when compared to crosslinked aerogel core but it resisted higher deflection before failure.

ADVISER'S APPROVAL: Dr. Hongbing Lu